Published in final edited form as:
Peptides. 2014 October ; 60: 63–70. doi:10.1016/j.peptides.2014.07.024.

Dynamic PET and SPECT imaging with radioiodinated, amyloid-reactive peptide p5 in mice: A positive role for peptide dehalogenation

Emily B. Martin[a], **Stephen J. Kennel**[a,b], **Tina Richey**[a], **Craig Wooliver**[a], **Dustin Osborne**[b], **Angela Williams**[a], **Alan Stuckey**[b], and **Jonathan S. Wall**[a,b]

[a]Department of Medicine, University of Tennessee Medical Center, 1924 Alcoa Highway, Knoxville, TN 37920

[b]Department of Radiology, University of Tennessee Medical Center, 1924 Alcoa Highway, Knoxville, TN 37920

Abstract

Dynamic molecular imaging provides bio-kinetic data that is used to characterize novel radiolabeled tracers for the detection of disease. Amyloidosis is a rare protein misfolding disease that can affect many organs. It is characterized by extracellular deposits composed principally of fibrillar proteins and hypersulfated proteoglycans. We have previously described a peptide, p5, which binds preferentially to amyloid deposits in a murine model of reactive (AA) amyloidosis. We have determined the whole body distribution of amyloid by molecular imaging techniques using radioiodinated p5. The loss of radioiodide from imaging probes due to enzymatic reaction has plagued the use of radioiodinated peptides and antibodies. Therefore, we studied iodine-124-labeled p5 by using dynamic PET imaging of both amyloid-laden and healthy mice to assess the rates of amyloid binding, the relevance of dehalogenation and the fate of the radiolabeled peptide. Rates of blood pool clearance, tissue accumulation and dehalogenation of the peptide were estimated from the images. Comparisons of these properties between the amyloid-laden and healthy mice provided kinetic profiles whose differences may prove to be indicative of the disease state. Additionally, we performed longitudinal SPECT/CT imaging with iodine-125-labeled p5 up to 72 hours post injection to determine the stability of the radioiodinated peptide when bound to the extracellular amyloid. Our data show that amyloid-associated peptide, in contrast to the unbound peptide, is resistant to dehalogenation resulting in enhanced amyloid-specific imaging.

Corresponding author: Jonathan Wall, University of Tennessee Graduate School of Medicine, 1924 Alcoa Highway, Knoxville, TN 37920, Tel: +1 865-305-5447, jwall@utmck.edu.
emarti15@vols.utk.edu, skennel@utmck.edu, trichey@utmck.edu, dwooliver@utmck.edu, dosborne@utmck.edu, awilliams@utmck.edu, astuckey@utmck.edu

Conflicts of Interest

SJK and JSW have patent rights associated with the use of peptides for amyloid imaging. SJK, EBM, TR, AS and JSW are part owners of a company that has licensed intellectual property associated with the use of peptides for amyloid imaging.

These data further support the utility of this peptide for detecting amyloidosis and monitoring potential therapeutic strategies in patients.

Keywords

Amyloid imaging; Peptide radiotracer; Dynamic PET imaging; SPECT; dehalogenation

1. Introduction

Amyloidosis is a protein misfolding disorder which can potentially affect all visceral organs. The amyloid in affected organs deposits extracellularly and is composed of hyper sulfated heparan sulfate proteoglycan (HSPG) and proteinaceous fibrils in association with the glycoprotein serum amyloid P component (SAP) and apolipoproteins [20, 23, 24]. Clinical diagnosis is reliant upon histochemical evaluation of invasive, biopsy-derived tissue samples that may not be representative of the whole organ [25]. Due to these limitations, we have studied molecular imaging with amyloidophilic radiotracers as a non-invasive alternative to detect and monitor disease progression and regression. Positron emission tomography (PET) and single photon emission computed tomography (SPECT) are clinically widespread imaging modalities that can be used, with the appropriate amyloid-targeting radiotracer, for visualizing amyloid deposits throughout the body. Molecular imaging has the potential to visualize, quantitatively and non-invasively, the whole body amyloid burden, making it an attractive alternative to serial biopsy which is prone to sampling error and clinical complications [35]. Currently, molecular imaging in the form of gamma scintigraphy is routinely used in certain amyloid imaging centers in Europe [8-11]. The radiotracer, Iodine-123-labeled serum amyloid P component (^{123}I-SAP), has been shown to detect amyloid in patients with secondary, reactive amyloidosis (AA), hemodialysis-related β-2 microglobulin amyloidosis, familial amyloid polyneuropathy (FAP) and light chain amyloidosis (AL) [11, 13, 19, 27].

However, ^{123}I-SAP scintigraphy does not effectively image cardiac or renal amyloid, is low resolution, non-quantitative, and the tracer is not an approved imaging agent in the United States. Therefore, alternative strategies are still being sought. We have identified a synthetic, amyloidophilic peptide p5 which has been shown, in preclinical dual-energy SPECT imaging studies, to detect amyloid deposition in a murine model of AA amyloidosis as effectively as the clinical gold standard imaging agent, SAP [35]. Peptide p5 is a 31- amino acid, non-natural, heparin-binding peptide with a heptad repeat Lys-X-X-Lys-X-X-X (X is Ala or Gln) providing a +8 net positive charge (Fig. 1). We have postulated that the interaction of peptide p5 with amyloid is due to electrostatic interactions between the unique, hyper-sulfated HSPG found in all amyloid deposits as well as the electronegative amino acid side chains of the fibrils themselves [16, 36]. The predicted secondary structure of p5 is α-helical in which the eight positively charged Lys residues (red), align on one face of the peptide (Fig. 1); this structure facilitates its interaction with negatively charged, sulfated glycosaminoglycans (GAGs) and acidic side chains on the amyloid associated HSPG and protein fibril, respectively [16, 36].

Peptides are particularly suited as radiotracers for molecular imaging because: they typically have high affinity and specificity for their target; they are easier to synthesize and characterize as compared to larger biomolecules such as antibodies; their smaller size can expedite clearance from the blood pool and off-target tissues, thereby rapidly enhancing signal-to-noise ratios and lowering the radiation dose to the patient [15]. At present, the growth in peptide radiotracer development is dramatic, and radiolabeled peptides such as the Arg-Gly-Asp (RGD) peptide and Octreotide (Sandostatin™, Novartis) are in routine clinical use for imaging and monitoring integrin and somatostatin receptor expression associated with angiogenesis and various cancerous tumors, respectively [4, 6, 15, 18]. In most cases, peptides are labeled with technetium-99m (^{99m}Tc) or fluorine-18 (^{18}F) for SPECT or PET imaging, respectively. Although common, these methods often require chelating moieties (that usually utilize the ε-amino group of lysyl residues) or are complex and inefficient – as in the case of ^{18}F peptide labeling [22]. Peptide p5 has been studied in vivo after radioiodination (^{125}I or ^{123}I for SPECT, and ^{124}I for PET) using a facile oxidative incorporation into the hydroxyphenol moiety of Tyr [33-36]. In preparation for translation of radioiodinated peptide p5 into clinical trials, we have characterized the kinetics of amyloid binding and clearance in vivo and, in particular, the effect of peptide dehalogenation.

2. METHODS

2.1. Animals

AA amyloidosis was induced in H2-L^{d}-HuIL-6 Tg BALB/c mice as previously described [34]. Briefly, the constitutive expression of the pro-inflammatory cytokine human interleukin 6 (IL-6) in these mice in combination with the intravenous (IV) administration of ~10 μg of amyloid enhancing factor (AEF) at 8 weeks of age caused rapid induction of amyloid deposition by 3 weeks post-AEF injection [31]. Mice used in these experiments were 6 weeks post induction. All animal procedures were conducted in accordance with protocols approved by the University of Tennessee Animal Care and Use Committee. This institution is accredited by the American Association for the Accreditation of Laboratory Animal Care-International.

2.2. Peptide synthesis and purification

Peptide p5, GGGYS KAQKA QAKQA KQAQK AQKAQ AKQAK Q, was purchased with free N- and C-termini (Keck Laboratories, New Haven, CT) as a crude < 80% pure preparation. The peptide was purified by reverse phase HPLC using a C3 matrix and acetonitrile gradient in 0.05% trifluoroacetic acid in water. The peptide eluted as a single peak from the column, and the mass of the purified material was confirmed by mass spectrometry. In all cases, the mass of the purified product was identical to thetheoretical mass +/− 3 units, indicating a lack of significant impurities. The peptide was lyophilized and stored at −20°C until used.

2.3. Radioiodination of the peptide for PET imaging

Due to the high energy gamma photons emitted by ^{124}I the preparation becomes oxidized. Therefore, peptide p5 was radiolabeled with ^{124}I (IBA Molecular, Sterling, WV) using Iodogen (Pierce chemical, Rockford, IL) oxidation following addition of ascorbic acid, as

described below [29]. Briefly, 10 μL of 0.5 M $NaPO_4$ buffer pH 7.6 was added to a 1.5 mL microcentrifuge tube before the addition of ~50 μL of ^{124}I (~ 2 mCi). One μL of 2 mg/mL fresh ascorbic acid solution in phosphate buffered saline (PBS) was added to ensure reduction of $^{124}I_2$. Approximately 25 μL (~ 50 μg) of peptide dissolved in distilled H_2O was mixed with ~75 μL of PBS and added to the reaction mixture. Seven μL of 1 mg/mL Iodogen dissolved in acetonitrile was added to initiate the reaction. After 2 min, the reaction was quenched with 50 μL of 2 mg/mL ascorbic acid. Twenty μL of blue dextran and 50 μL of filtered (0.2 μm pore sized) 0.1 % gelatin in PBS were added to the reaction mixture. Radiolabeled product was separated from free ^{124}I by size exclusion chromatography using a PD10 matrix (GE Healthcare) equilibrated with 2 bed volumes (~ 10 mL) of 0.1 % filtered gelatin in PBS. Fractions were manually collected as the blue dextran marker reached the base of the column and the radioactivity in each measured using a dose calibrator (Capintec, Model 15, Ramsey, NJ) set for ^{124}I detection. Peak fractions were pooled for use in the study. Radiochemical purity was assessed with SDS polyacrylamide gel electrophoresis (PAGE) analyzed by phosphor imaging (Cyclone Storage Phosphor System, Perkin Elmer, Shelton, CT).

2.4. Radioiodination of the peptide for SPECT imaging

Radioiodination of the peptide with ^{125}I (Perkin Elmer, Waltham, MA) using chloramine T was performed as previously described, without modification [36].

2.5. Dynamic PET/CT imaging of ^{124}I-p5 in mice

2.5.1. PET image acquisition—Mice (healthy and amyloid laden, n = 3 per group) were anesthetized in an induction chamber by exposure to 3 % isoflurane in air before being maintained with 2% isoflurane administered via a nose-cone for placement of a IV catheter in the lateral tail vein. Anesthetized mice were positioned in a heated imaging chamber (M2M, Cleveland, OH). PET/CT imaging was performed using an Inveon trimodality SPECT/PET/CT platform (Siemens Preclinical Solutions, Knoxville, TN) running Inveon Acquisition Workplace software (ver. 1.5). Dynamic PET data acquisition was initiated ~5 sec prior to injection of the radiotracer. The mice received ~20 μg of ^{124}I-p5 (~400 μCi) in ~200 μL gelatin/PBS solution with 1 mM ethylenediaminetetraacetic acid. The PET data were acquired for 2 h and then histogrammed for ^{124}I. The data were reconstructed into the following bins: 10 × 1 sec, 10 × 30 sec, 30 × 114 sec, and 60 frames covering the remainder of the data. The PET data were corrected for attenuation and scatter by using the CT dataset. PET data were reconstructed using a 3D ordered subset expectation maximization with maximum a posteriori algorithm. The image matrix was 256 × 256 × 159 with a reconstructed pixel size of 0.0215 × 0.0215 × 0.796 mm.

2.5.2. CT image acquisition—CT data were acquired over two bed positions using an X-ray voltage biased to 80 kVp an anode current of 500 μA. A total of 121 projections with 225 ms exposure were collected covering 220° of continuous rotation with low magnification and binning set at 4. The data were reconstructed using an implementation of the Feldkamp-filtered back-projection algorithm onto a 224 × 224 × 635 matrix with isotropic 212.1-μm voxels.

2.6. SPECT/CT imaging of ^{125}I-p5 in mice

SPECT imaging was performed as previously described [36] with slight modifications. Amyloid-laden mice were injected with ~5 μg ^{125}I-p5 (~150 μCi) in the lateral tail vein. After the appropriate uptake time (2 h, 24 h, 48 h, or 72 h pi), mice were administered anesthesia under the same conditions (as described in 2.4.1) prior to positioning on the Inveon imaging system (Siemens Preclinical Solution).

The SPECT data acquisition was set to detect low energy gamma photons (^{125}I; 25 – 45 keV) at each of 60, 16-sec projections with 90 mm of bed travel. The multi-pinhole (Mouse Whole Body) collimator was used with a 30 mm radius of rotation. Data were reconstructed using a 3D ordered subset expectation maximization (OSEM) algorithm (8 iterations; 6 subsets) onto an 88 × 88 × 312 matrix with isotropic 0.5 mm voxels. The CT data were acquired as described in Section 2.4.2.

Imaging of free ^{125}I (~ 100 μCi) in WT mice was performed at 30 min post injection using a microSPECT/CT II, as described [30]. Image analysis was performed using Amira software package, as previously described [30].

2.7. Dynamic PET image analysis

PET image data were co-registered with the CT image data using the Inveon Research Workplace 2D visualization software package (IRW: Siemens Preclinical Solution: Knoxville, TN). All image frames were summed and regions of interest (ROI) encompassing 2-3 slices were drawn over the vena cava, heart, liver, spleen, kidneys, stomach and bladder of each mouse. Time activity curves for each ROI were generated with the IRW kinetic analysis tool. These data were then further analyzed by fitting to simple exponential equations using Prism ver 6.0 (GraphPad Software Inc, La Jolla, CA).

2.8. SPECT/CT image analysis

SPECT image data were co-registered with the CT data using IRW. Image analysis was performed by drawing ROIs over the liver, spleen, pancreas, heart, lung, muscle, stomach, bladder, intestines and kidneys. The mean voxel intensity associated with each ROI was noted and used to compare the ROIs from all imaging time points. The initial 2 h time point measurements were recorded as 100 percent peptide binding. All other time points were scaled to the initial and expressed as % change relative to the initial image.

2.9. Dynamic analysis of tissue radioactivity

Groups of 2 wild type mice each received 95 μCi of ^{125}I-p5 IV in the lateral tail vein. Animals were euthanized at 1, 5, 15, 30 and 60 min post injection and the kidneys and blood harvested during necropsy. Samples of each (~5 mg) were homogenized and boiled in SDS-PAGE sample buffer for 10 min, and a sample of the resulting supernatant, following brief centrifugation, was examined by SDS-PAGE. Radiolabeled peptide and ^{125}I were visualized by using a phosphorimager as described (Section 2.3). Purified ^{125}I-p5 peptide served as a control on the gels. The density of the peptide and free ^{125}I bands was quantified using the Optiquant software package (ver. 5.0.0.2, Perkin Elmer).

2.10. Microautoradiography

The microautoradiography of harvested tissues has been previously described [34]. Briefly, mice were euthanized after the final image-acquisition by isoflurane overdose in a closed chamber. Tissues were harvested and fixed for 24 hours in 10% buffered formalin before being embedded in paraffin. Six μm-thick sections were cut onto microscope slides, dipped in NTB-2 emulsion (Eastman Kodak) and stored in the dark. Slides were developed after a 96 hour exposure and counterstained with hematoxylin. All tissues were examined using a Leica DMR light microscope, and digital images were captured using a SPOT camera and software (Diagnostic Instruments, Sterling Heights, MI).

2.11. Detection of tissue amyloid using Congo red fluorescence

To confirm the presence of amyloid, consecutive tissue sections from those used for microautoradiography were stained with freshly prepared alkaline Congo red [31]. The tissues were examined using a Leica DMR using epifluorescent illumination and a rhodamine filter.

2.12. Biodistribution

The distribution of radioiodinated peptide in tissues harvested at necropsy was performed as previously described [34]. Data are presented as percent injected dose per gram of tissue (%ID/g).

3. Results

The structure of p5 was predicted by using the I-Tasser modeling software [38] to be α-helical (Fig. 1A). The basic, Lys amino acid side chains (red) are predicted to align on one side of the helix (Fig. 1B).

3.1. Analysis of PET images

To determine the kinetic parameters related to the distribution and uptake of p5 in vivo, dynamic PET imaging using ^{124}I-p5 peptide was performed. PET data acquired between 0 – 5 min pi were summed, and the images showed that, in AA mice, ^{124}I-p5 was accumulating within the liver (L) and intestines (I) in greater amounts relative to WT mice (Fig. 2A). In contrast, the heart (H; a surrogate for blood pool in the image data) appeared to have more radioactivity in WT, as compared to AA mice, at this early time point (Fig. 2A; 5 min). After 30 mins, however, the peptide was clearly seen localized to the liver and spleen (S) of the AA mice with activity also visible in the intestines (Fig 2A). In contrast, the ^{124}I-p5 peptide in WT mice was observed in the liver and heart with equal intensity. The stomach and thyroid were also seen to accumulate radioactivity (indicative of uptake of free radioiodide liberated during catabolism and dehalogenation of the peptide). This trend continued such that, by 120 min pi, the distribution of radioactivity in the WT and AA mice was dramatically different in the PET images (Fig. 2A). Notably, there was significant radioactivity in the liver, intestines and spleen of the AA mice; whereas the blood pool, stomach and thyroid were evident in the WT mice (Fig. 2A; 120 min).

3.2. Analysis of time activity curves from PET data: Visceral organs

Time activity curves (TAC) for the heart (surrogate for blood pool), kidney, stomach, liver, spleen and thyroid were generated from the dynamic PET data in order to parameterize the peptide uptake, clearance and dehalogenation in healthy and amyloid-laden mice (Fig. 2B). Radioactivity within the blood pool cleared quickly in both AA and WT mice with a biexponential decay (Table 1); however, the K_{fast} (α component) and K_{slow} (β) were > 2-fold higher in the AA mice. There was a notable kinetic event in the TAC of the WT blood indicated by an arrow (Fig. 2B, Blood, inset), which resulted in a slightly less efficient fit of this data to a biexponential decay ($R^2 = 0.988$) as compared to that of the AA mouse data ($R^2 = 0.995$). The activity in the kidneys peaked (t_{max}) at ~ 7 min in WT mice and then began to decrease according to a single exponential decay ($R^2 = 0.992$) with K_{fast} of 0.06 min^{-1}. In contrast, the radiotracer behaved differently within the kidneys of amyloid-laden mice showing little accumulation or clearance (0.04 min^{-1}; Table 1). The liver and spleen, sites of significant AA amyloid deposition in these mice, were characterized by TACs that indicated accumulation of ^{124}I-p5 in AA mice (exponential association), whereas in WT mice, the kinetics were described by exponential decays (Table 1).

3.3. Analysis of time activity curves from PET data: Dehalogenation

Radioiodide was liberated during the catabolism and dehalogenation of the peptide in the liver and, principally, kidneys. This was evidenced by the rapid sequestration of radioactivity by the stomach and thyroid (Fig. 2B). Both WT and AA stomach TACs were characterized by a lag time (t_{lag} of ~ 8 min) before rapid and linear accumulation of radioactivity; however, the rate of accumulation in the WT (63,917 Bq/ml/min; $R^2 = 0.998$) stomach was ~ 8-fold faster than that of the AA mice (8,125 Bq/mL/min; $R^2 = 0.95$). The thyroid radioactivity also had a t_{lag} of ~ 8 min; however, only the WT TAC could be reasonably described by a single exponential rate constant (0.03 min^{-1}; $R^2 = 0.993$) as compared to the AA ($R^2 = 0.43$), and therefore, rate constants were not determined (nd; Table 1).

3.4. Tissue biodistribution of ^{124}I radioactivity

The biodistribution of radioactivity in selected tissues, expressed as the percent injected dose per gram of tissue (%ID/g), was determined for AA and WT mice ($n = 3$) at the end of the dynamic PET imaging protocol (Fig. 2C). In general, these data correlate well with the mouse images at 120 min pi. There was ~ 10 fold more radioactivity in the major sites of amyloid: the liver, pancreas and spleen of AA mice as compared to the WT mice (Fig. 2C).

3.5. Microautoradiography of ^{124}I-p5 in tissue sections

To confirm that the ^{124}I-p5 within the liver and spleen was specifically co-localized with discrete amyloid deposits, we performed microautoradiography (Fig. 2D). The black grains deposited in the tissues, due to the presence of ^{124}I-p5 (Fig. 2D; upper), correlated spatially with the Congo red fluorescence signal indicative of the presence of AA amyloid (Fig. 2D; lower). These data also demonstrated that the ^{124}I-labeled p5 peptide did not bind to healthy (amyloid-free) regions of the liver, kidney, adrenal and all other tissues examined (data not shown).

3.6. Dynamic distribution of free ^{125}I in WT mice

Free ^{125}I (arrowhead; •) liberated during catabolism of the ^{125}I-labeled p5 (arrow; ○) was visualized by phosphorimaging of SDS-PAGE gels and peaked in the blood at ~ 15-30 min post injection, coincident with the “perturbation” seen in the TAC (Fig. 2B, blood inset). In contrast, the radiolabeled peptide decreased rapidly, consistent with the dynamic PET imaging (Figs. 3A & B). In the kidney, the peptide and free ^{125}I exhibited identical kinetic patterns over the 60 min study period (Figs. 3C & D), consistent with ^{125}I rapidly exiting the kidney into the blood. SPECT/CT imaging of free ^{125}I in WT mice was used to confirm that the thyroid (T) and stomach (St) were the major sites of uptake in mice at 30 min post injection (Fig. 3E).

3.7. Longitudinal SPECT imaging of ^{125}I-p5

Dynamic PET imaging had demonstrated that the p5 peptide rapidly binds AA amyloid deposits in vivo (Section 3.3); however, these data did not address the stability of the radiolabeled peptide once bound to amyloid. To investigate this, we performed longitudinal SPECT/CT imaging with repeated imaging of individual AA mice at 2 h, 24 h, 48 h and 72 h pi of ^{125}I-p5. The extended half-life of ^{125}I (59.6 days) is amenable to this type of long-term study. The ^{125}I-p5 was retained in the liver and spleen for more than 72 h pi, as evidenced in representative SPECT/CT images (Fig. 4A). The SPECT mean voxel intensities for ROI in the liver, spleen, pancreas, heart, lung, muscle, stomach, bladder, intestines and kidney were obtained (Fig. 4B). The radioactivity at each time point was expressed as a % change relative to the initial measurement at 2 h pi (representing 100 percent). These data further indicated that amyloid-laden organs— liver, spleen, pancreas and kidneys—retained ~75 - 100% of the ^{125}I-labeled p5 peptide for more than 72 h pi. In contrast, organs with less AA amyloid, such as the heart, stomach and intestines, saw dramatic reductions in tissue radioactivity in the first 24 h pi but then stabilized at 10-20% of the initial measurement (Fig. 4B).

3.8. Microautoradiography of ^{125}I-p5 in tissue sections

The specificity of the reactivity of the ^{125}I-p5 at 72 h pi with amyloid was similarly assessed microautoradiographically (section 3.5). Autoradiographs of the liver, spleen, kidney, heart and pancreas were developed from the mice at 72 h pi (Fig. 5, upper). The distribution of the ^{125}I-p5 peptide, evidenced by the deposition of black silver grains, coincided precisely with the AA amyloid shown by Congo red fluorescence microscopy (Fig. 5, lower). No significant reactivity was seen with healthy tissues, even at 72 h pi.

4. Discussion

4.1. Amyloidosis and amyloid imaging

Amyloidosis is a devastating protein pathology associated with numerous disorders including Alzheimer’s disease, type 2 diabetes, multiple myeloma and chronic inflammation [17, 21]. The incessant deposition of amyloid destroys tissue architecture leading to dysfunction and death. In patients with peripheral (i.e., non-cerebral) amyloidosis, notably light chain (AL) and reactive (AA) amyloidosis, renal involvement is prevalent, debilitating

and results in poor prognosis; therefore, early detection is an important clinical need. Methods for quantitatively detecting the whole-body amyloid burden in patients with peripheral disease are necessary for prognostication, treatment planning and monitoring response to therapy.

Radiolabeled SAP is available and routinely used for amyloid imaging in Europe to visualize the extent of peripheral amyloidosis; however, it has not been approved by the Food and Drug Administration for use in the US, and it is not amenable to quantitative imaging, especially of amyloid in the heart and kidneys. In addition, we and others have shown that newly developed probes for Aβ amyloid associated with Alzheimer's disease are not optimal for routine visualization and quantitation of peripheral amyloid diseases. Thus, there remains a critical need for peripheral amyloid imaging agents. We have studied a variety of heparin-binding peptides [34, 36] that may be useful for this purpose. Central to the development of an efficient imaging probe is the choice of isotope and radiochemistry involved in preparation.

4.2. Peptide p5 as an amyloid imaging agent

Synthetic peptides are well-suited as tracers for molecular imaging. They possess: good binding specificity to the target; rapid clearance from the circulation (leading to rapid optimization of the signal-to-noise ratios and acceptable patient dosimetry); and relatively facile radiolabeling by direct radioiodination or by using radionuclide chelators that can be incorporated quantitatively during peptide synthesis. Furthermore, when compared to other biological reagents, such as antibodies, peptides can be more readily translated into man principally because they can be chemically synthesized and do not require biological expression systems. Peptide p5 is a non-natural, 31 amino acid, heparin-binding peptide with a net charge of +8 [12, 26, 34]. It binds heparin with a ~ 0.64 μM affinity [36] and is predicted to adopt an α-helical structure that aligns the basic lysyl side chains on one face of the helix [26, 36]. When radiolabeled, peptide p5 has been shown in vitro and in the murine model of AA amyloidosis to bind preferentially to the tissue amyloid deposits in a quantitative fashion relative to the amyloid load estimated by Congo red staining [33]. Binding to amyloid results from electrostatic interactions with both hypersulfated GAGs and protein fibrils in the deposits. We have also demonstrated using biotinylated p5 peptides that this reagent is capable of binding many human amyloid deposits by using histochemical techniques [16, 34].

To construct p5, the original heparin binding sequence (residues 5 – 31) was synthesized with a Gly-Gly-Gly-Tyr-amino acid sequence at the N terminus. This peptide was readily radioiodinated via direct oxidative (either Chloramine T or Iodogen) incorporation of iodide to the ortho or para positions of the Tyr hydroxyphenol moiety. This is a facile and well characterized radiolabeling technique for proteins and peptides and allows generation of variants for preclinical testing, clinical SPECT, and clinical PET imaging, using ^{125}I, ^{123}I, and ^{124}I, respectively. Although popular, this method results in moieties that are prone to dehalogenation in vivo due to their recognition by Type 1 deiodinases present in the liver and kidney, in particular [3]. Strategies, notably the use of succinimidyl-iodobenzoate (SIB), have been adopted to address dehalogenation since ortho or para iodobenzoic acid is not

recognized by the dehalogenase enzymes [7]; however, this relies on incorporation of SIB onto ε amino groups of Lys residues which, in p5, are critical for the amyloid reactivity.

As evidenced in our dynamic PET studies, ^{124}I-p5 was rapidly cleared from the blood pool with ~ 90% of the radioactivity removed by 5 min pi (Fig. 2B). In mice with AA amyloid, the peptide was bound by the amyloid in the liver, spleen, intestines, pancreas and other sites. In contrast, in amyloid-free WT mice, the peptide was rapidly cleared through the kidney with a peak uptake time (t_{max}) of ~ 7 min pi. The renal radioactivity then decreased, which would normally be associated with transit of the reagent to the bladder; however, in this case, at least part of the decrease in ^{124}I in the kidney was due to dehalogenation of the peptide and liberation of free radioiodide back into the circulation. This was manifest as a small increase in the blood radioactivity at ~ 16 min pi. Free iodide re-entering the circulation at this time point was confirmed by using SDS-PAGE analysis of timed blood sample collections following IV injection of ^{125}I-p5 (Fig. 3). The free radioiodide was transiently sequestered by halide transporters in the stomach resulting in a rapid increase in radioactivity in this organ. The ^{124}I, likely localized to the parietal cells of the stomach, was converted to H^{124}I and entered the lumen of the stomach before being excreted via the intestines. This process is far more efficient than the organification of ^{124}I in the thyroid as evidenced by the difference in the rate of uptake by these two organs over 120 min pi. It may be that the stomach, due to its larger mass, dominates the removal of iodide from the circulation, or it could be due to the relative expression of halide transport proteins in the thyroid (Na/I symporters) and the stomach (numerous chloride channel transporters [2]).

The radioiodinated p5, when bound to extracellular amyloid, was shown to be resistant to dehalogenation (see Fig. 4B) which presumably occurs intracellularly, perhaps by Type 1 deiodinases that are present in the basolateral membrane of kidney cells with the enzymatic center in the cytosol [14]. This process may also be dependent upon uptake of the peptide by the cubulin-megalin scavenger system present on renal proximal tubule cells [5].

Indeed, the peptide (^{125}I-p5) was readily imaged at 72 h pi in mice with essentially no loss of radioactivity from the major amyloid organs in these animals (liver, spleen and pancreas). This contrasts dramatically with small molecule imaging agents such as Amyvid™ (^{18}F-AV-45; florbetapir) and Flutemetamol™ (^{18}F-GE-067; ^{18}F-PIB), designed principally for Aβ amyloid detection in the brains of patients with Alzheimer's disease [28, 37]. Both of these agents have been shown, by dynamic PET imaging and parametric analysis of the image data, to identify patients with cardiac amyloidosis; however, the transient association of these reagents makes routine, equilibrium visualization of peripheral amyloid and quantitation of amyloid load improbable [1].

Our data (Fig. 4) demonstrate that amyloid-bound, iodinated peptide could be imaged many days pi, whereas unbound peptide that was rapidly cleared principally through the kidney was dehalogenated becoming undetectable by imaging in a few hours. The exception is the thyroid accumulation which persists, but it does not complicate amyloid detection in other organs.

Therefore, rapid dehalogenation of unbound peptide and sequestration and elimination of radioiodide by the stomach enhances the visual detection of amyloid by imaging. It is of interest to note that radioiodinated peptide bound to kidney and stomach amyloid is not dehalogenated; thus, at appropriate times pi (> 2 h, in mice), the amyloid in these sites can be imaged and quantified using this technique. We have shown that, due to the excellent affinity of this peptide for amyloid, the clearance period can be many days pi, and isotopes such as ^{123}I (13 h half-life) for SPECT imaging and ^{124}I (4.2 d half-life) for PET imaging are amenable for this purpose.

The rapid loss of imaging signal of unbound probe is advantageous in a clinical setting. The radiotracer could be injected and the patient imaged a day (or more) later to allow time for clearance of unbound peptide and liberated radioiodide which would lessen the background noise in the image. This imaging strategy was employed in a recent clinical trial using the amyloid fibril-reactive antibody, ^{124}I-11-1F4 [32]. This ability to wait extended periods of time pi without loss of positive, amyloid-related, signal and to allow background clearance, may also increase detection of renal amyloidosis and small amyloid deposits which may form early in the disease process. Thus, an extended “on-target” half-life and the rapid dehalogenation of unbound peptide with redistribution of the radioiodide are advantageous properties of ^{124}I-p5 for amyloid detection, particularly within the kidney – a critical organ for this disease.

5. Conclusion

The peptide p5 can be readily radioiodinated and used for the specific detection of tissue amyloid in mice by using high-resolution small animal SPECT and PET imaging. The peptide binds rapidly to amyloid deposits and remains stably bound and radioactive for at least 72 h pi. In contrast, unbound peptide is cleared through the kidneys. The peptide is rapidly dehalogenated, and the liberated free radioiodide is redistributed through the circulation to the stomach and thyroid resulting in rapid clearance from the imaging fields of interest. Taken together, these properties render ^{124}I-p5 peptide a good candidate for the quantitative detection of peripheral amyloid in patients, especially the scant, but clinically important, deposits in the kidneys.

Acknowledgments

This work was supported by PHS grant R01DK079984 from The National Institute of Diabetes and Digestive and Kidney Diseases (NIDDK). We thank Jim Wesley for his expertise in preparing the microautoradiographs.

Abbreviations

PET	positron emission tomography
SPECT	single photon emission computed tomography
CT	x-ray computed tomography
AA	reactive (serum amyloid protein A) amyloidosis
HSPG	heparan sulfate proteoglycan

GAG	glycosaminoglycans
SAP	serum amyloid P-component
FAP	familial amyloid polyneuropathy
AL	light chain amyloidosis
AEF	amyloid enhancing factor
ROI	region of interest
TAC	time activity curve
SIB	succinimidyl-iodobenzoate
ARG	microautoradiograph
CR	Congo red
pi	post injection

References

[1]. Antoni G, Lubberink M, Estrada S, Axelsson J, Carlson K, Lindsjo L, et al. In vivo visualization of amyloid deposits in the heart with 11C-PIB and PET. Journal of nuclear medicine: official publication, Society of Nuclear Medicine. 2013; 54:213–20.

[2]. Aoyama F, Sawaguchi A. Functional transformation of gastric parietal cells and intracellular trafficking of ion channels/transporters in the apical canalicular membrane associated with acid secretion. Biological & pharmaceutical bulletin. 2011; 34:813–6. [PubMed: 21628877]

[3]. Araujo RL, Carvalho DP. Bioenergetic impact of tissue-specific regulation of iodothyronine deiodinases during nutritional imbalance. Journal of bioenergetics and biomembranes. 2011; 43:59–65. [PubMed: 21249435]

[4]. Chin FT, Shen B, Liu S, Berganos RA, Chang E, Mittra E, et al. First experience with clinical-grade ([18F]FPP(RGD(2)): an automated multi-step radiosynthesis for clinical PET studies. Molecular imaging and biology: MIB: the official publication of the Academy of Molecular Imaging. 2012; 14:88–95. [PubMed: 21400112]

[5]. Christensen EI, Birn H, Storm T, Weyer K, Nielsen R. Endocytic receptors in the renal proximal tubule. Physiology. 2012; 27:223–36. [PubMed: 22875453]

[6]. Gaertner FC, Kessler H, Wester HJ, Schwaiger M, Beer AJ. Radiolabelled RGD peptides for imaging and therapy. European journal of nuclear medicine and molecular imaging. 2012; 39(Suppl 1):S126–38. [PubMed: 22388629]

[7]. Garg PK, Alston KL, Welsh PC, Zalutsky MR. Enhanced binding and inertness to dehalogenation of alpha-melanotropic peptides labeled using N-succinimidyl 3-iodobenzoate. Bioconjugate chemistry. 1996; 7:233–9. [PubMed: 8983345]

[8]. Hawkins PN. Diagnosis and monitoring of amyloidosis. Bailliere's clinical rheumatology. 1994; 8:635–59.

[9]. Hawkins PN. Serum amyloid P component scintigraphy for diagnosis and monitoring amyloidosis. Current opinion in nephrology and hypertension. 2002; 11:649–55. [PubMed: 12394612]

[10]. Hawkins PN, Pepys MB. Imaging amyloidosis with radiolabelled SAP. European journal of nuclear medicine. 1995; 22:595–9. [PubMed: 7498219]

[11]. Hazenberg BP, van Rijswijk MH, Piers DA, Lub-de Hooge MN, Vellenga E, Haagsma EB, et al. Diagnostic performance of 123I-labeled serum amyloid P component scintigraphy in patients with amyloidosis. The American journal of medicine. 2006; 119:355e15–24. [PubMed: 16564782]

[12]. Jayaraman G, Wu CW, Liu YJ, Chien KY, Fang JC, Lyu PC. Binding of a de novo designed peptide to specific glycosaminoglycans. FEBS letters. 2000; 482:154–8. [PubMed: 11018540]

[13]. Ketteler M, Koch KM, Floege J. Imaging techniques in the diagnosis of dialysis-related amyloidosis. Seminars in dialysis. 2001; 14:90–3. [PubMed: 11264773]

[14]. Leonard JL, Ekenbarger DM, Frank SJ, Farwell AP, Koehrle J. Localization of type I iodothyronine 5′-deiodinase to the basolateral plasma membrane in renal cortical epithelial cells. The Journal of biological chemistry. 1991; 266:11262–9. [PubMed: 2040632]

[15]. Liu Y, Tian M, Zhang H. Microfluidics for synthesis of peptide-based PET tracers. BioMed research international. 2013; 2013:839683. [PubMed: 24288688]

[16]. Martin EB, Williams A, Heidel E, Macy S, Kennel SJ, Wall JS. Peptide p5 binds both heparinase-sensitive glycosaminoglycans and fibrils in patient-derived AL amyloid extracts. Biochemical and biophysical research communications. 2013; 436:85–9. [PubMed: 23707811]

[17]. Merlini G, Bellotti V. Molecular mechanisms of amyloidosis. The New England journal of medicine. 2003; 349:583–96. [PubMed: 12904524]

[18]. Mittra ES, Goris ML, Iagaru AH, Kardan A, Burton L, Berganos R, et al. Pilot pharmacokinetic and dosimetric studies of (18)F-FPPRGD2: a PET radiopharmaceutical agent for imaging alpha(v)beta(3) integrin levels. Radiology. 2011; 260:182–91. [PubMed: 21502381]

[19]. Nelson SR, Hawkins PN, Richardson S, Lavender JP, Sethi D, Gower PE, et al. Imaging of haemodialysis-associated amyloidosis with 123I-serum amyloid P component. Lancet. 1991; 338:335–9. [PubMed: 1677697]

[20]. Nelson SR, Lyon M, Gallagher JT, Johnson EA, Pepys MB. Isolation and characterization of the integral glycosaminoglycan constituents of human amyloid A and monoclonal light-chain amyloid fibrils. The Biochemical journal. 1991; 275(Pt 1):67–73. [PubMed: 1902087]

[21]. Obici L, Perfetti V, Palladini G, Moratti R, Merlini G. Clinical aspects of systemic amyloid diseases. Biochimica et biophysica acta. 2005; 1753:11–22. [PubMed: 16198646]

[22]. Olberg DE, Hjelstuen OK. Labeling strategies of peptides with (1)(8)F for positron emission tomography. Current topics in medicinal chemistry. 2010; 10:1669–79. [PubMed: 20583991]

[23]. Pepys MB. Amyloidosis. Annual review of medicine. 2006; 57:223–41.

[24]. Pepys MB, Rademacher TW, Amatayakul-Chantler S, Williams P, Noble GE, Hutchinson WL, et al. Human serum amyloid P component is an invariant constituent of amyloid deposits and has a uniquely homogeneous glycostructure. Proceedings of the National Academy of Sciences of the United States of America. 1994; 91:5602–6. [PubMed: 8202534]

[25]. Rocken C, Shakespeare A. Pathology, diagnosis and pathogenesis of AA amyloidosis. Virchows Archiv: an international journal of pathology. 2002; 440:111–22. [PubMed: 11964039]

[26]. Rullo A, Nitz M. Importance of the spatial display of charged residues in heparin-peptide interactions. Biopolymers. 2010; 93:290–8. [PubMed: 19885920]

[27]. Rydh A, Suhr O, Hietala SO, Ahlstrom KR, Pepys MB, Hawkins PN. Serum amyloid P component scintigraphy in familial amyloid polyneuropathy: regression of visceral amyloid following liver transplantation. European journal of nuclear medicine. 1998; 25:709–13. [PubMed: 9662592]

[28]. Vandenberghe R, Van Laere K, Ivanoiu A, Salmon E, Bastin C, Triau E, et al. 18 F-flutemetamol amyloid imaging in Alzheimer disease and mild cognitive impairment: a phase 2 trial. Annals of neurology. 2010; 68:319–29. [PubMed: 20687209]

[29]. Verel I, Visser GW, Vosjan MJ, Finn R, Boellaard R, van Dongen GA. High-quality 124I-labelled monoclonal antibodies for use as PET scouting agents prior to 131I-radioimmunotherapy. European journal of nuclear medicine and molecular imaging. 2004; 31:1645–52. [PubMed: 15290121]

[30]. Wall JS, Kennel SJ, Paulus M, Gregor J, Richey T, Avenell J, et al. Radioimaging of light chain amyloid with a fibril-reactive monoclonal antibody. Journal of nuclear medicine: official publication, Society of Nuclear Medicine. 2006; 47:2016–24.

[31]. Wall JS, Kennel SJ, Paulus MJ, Gleason S, Gregor J, Baba J, et al. Quantitative high-resolution microradiographic imaging of amyloid deposits in a novel murine model of AA amyloidosis. Amyloid: the international journal of experimental and clinical investigation: the official journal of the International Society of Amyloidosis. 2005; 12:149–56.

[32]. Wall JS, Kennel SJ, Stuckey AC, Long MJ, Townsend DW, Smith GT, et al. Radioimmunodetection of amyloid deposits in patients with AL amyloidosis. Blood. 2010; 116:2241–4. [PubMed: 20522711]

[33]. Wall JS, Richey T, Macy S, Heidel E, Wooliver C, Kennel SJ. A novel method for quantifying peripheral tissue amyloid load by using the radiolabeled amyloidophilic peptide, p5. Amyloid: the international journal of experimental and clinical investigation: the official journal of the International Society of Amyloidosis. 2013; 20:21–6.

[34]. Wall JS, Richey T, Stuckey A, Donnell R, Macy S, Martin EB, et al. In vivo molecular imaging of peripheral amyloidosis using heparin-binding peptides. Proceedings of the National Academy of Sciences of the United States of America. 2011; 108:E586–94. [PubMed: 21807994]

[35]. Wall JS, Richey T, Williams A, Stuckey A, Osborne D, Martin E, et al. Comparative analysis of peptide p5 and serum amyloid P component for imaging AA amyloid in mice using dual-isotope SPECT. Molecular imaging and biology: MIB: the official publication of the Academy of Molecular Imaging. 2012; 14:402–7. [PubMed: 22042488]

[36]. Wall JS, Williams A, Richey T, Stuckey A, Huang Y, Wooliver C, et al. A binding-site barrier affects imaging efficiency of high affinity amyloid-reactive Peptide radiotracers in vivo. PloS one. 2013; 8:e66181. [PubMed: 23750281]

[37]. Wong DF, Rosenberg PB, Zhou Y, Kumar A, Raymont V, Ravert HT, et al. In vivo imaging of amyloid deposition in Alzheimer disease using the radioligand 18F-AV-45 (florbetapir [corrected] F 18). Journal of nuclear medicine: official publication, Society of Nuclear Medicine. 2010; 51:913–20.

[38]. Zhang Y. I-TASSER server for protein 3D structure prediction. BMC bioinformatics. 2008; 9:40. [PubMed: 18215316]

Highlights

- Peptide p5 binds rapidly to amyloid in vivo and remains bound for at least 3 days.
- In contrast, radiolabeled p5 is rapidly cleared from healthy tissues.
- Dehalogenation of unbound p5 in the kidney allows for renal amyloid imaging.
- Radioiodinated p5 is suitable for imaging amyloid in vivo.

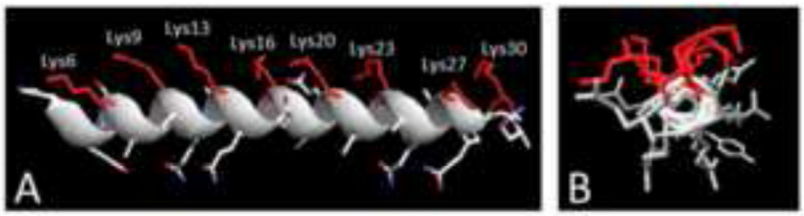

Figure 1.
The α-helical structure of peptide p5. A) The eight Lys side chains of p5 are aligned along one face of the α-helix. B) End-on view of p5 helix.

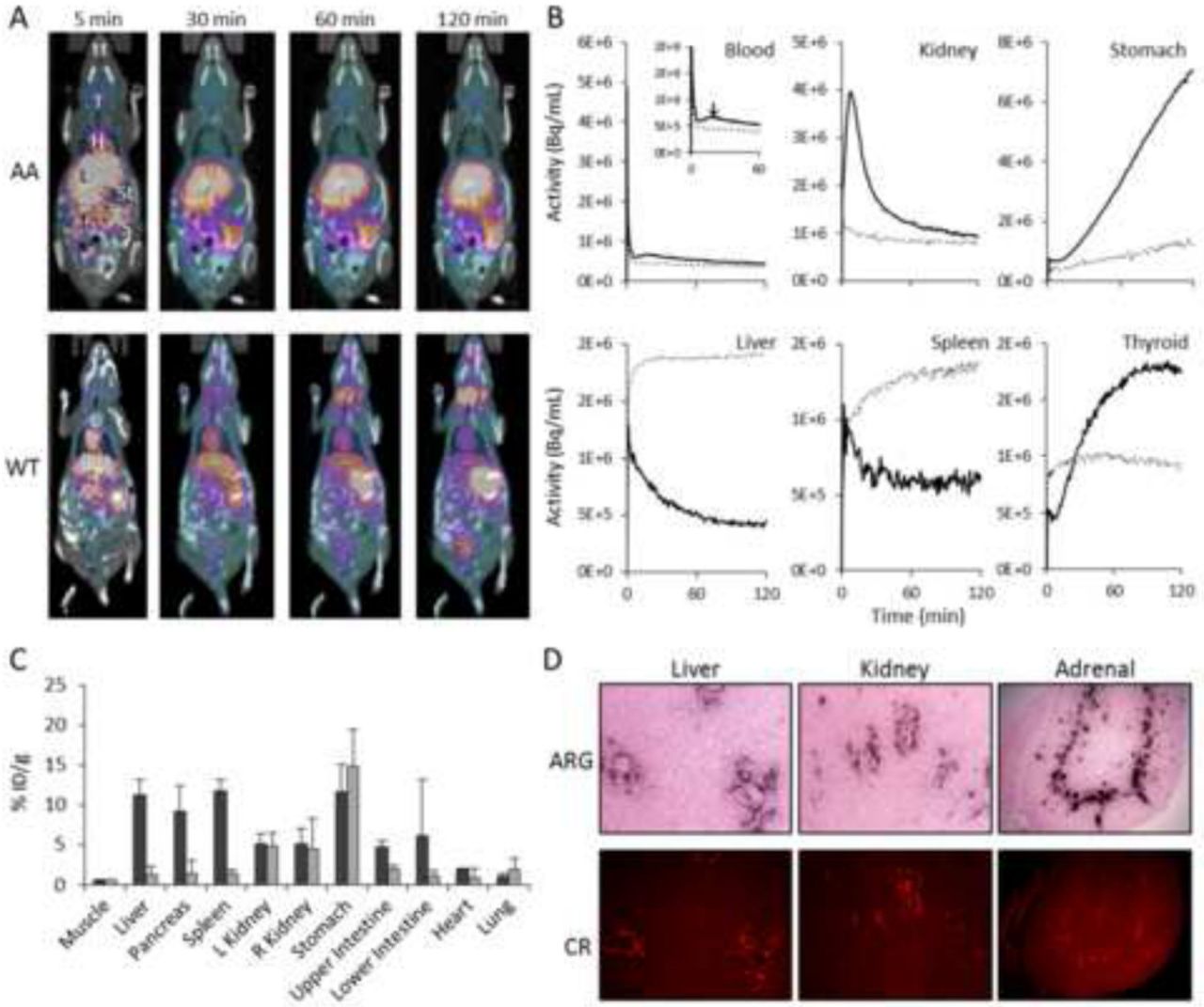

Figure 2.

Dynamic PET imaging of ^{124}I-p5 binding to amyloid in vivo. A) Whole body biodistribution of radioactivity by PET/CT imaging in AA and WT mice summed at 5, 30, 60 and 120 min pi, where L, liver, T, thyroid, St, stomach, S, spleen and I, intestines. Yellow and purple colors represent the presence of radioactivity. B) TAC data for the initial 120 mins post injection of ^{124}I-p5. ROI's were placed over tissues and the change in tissue radioactivity measured in mice with AA (dashed line) or WT (solid line: data represent mean of 3 mice). C) Tissue radioactivity measurements (%ID/g) measured at 120 min pi of ^{124}I-p5 in AA (dark) and WT (light) mice (mean ± SD, n = 3). D) Representative tissue microdistribution of ^{124}I-p5 at 120 min pi in microautoradiographs (ARG). Amyloid was detected by Congo red fluorescence (CR) in consecutive tissue sections.

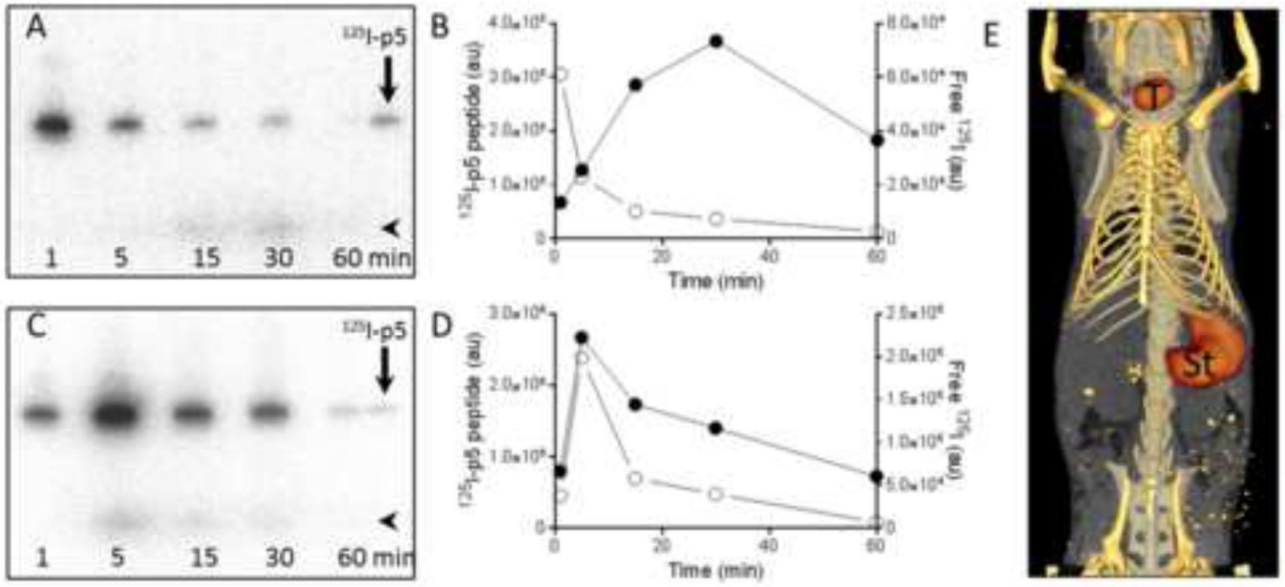

Figure 3.

Deiodination of ^{125}I-p5 results in free ^{125}I in the circulation and uptake in the stomach and thyroid in WT mice. SDS-PAGE phosphor images and quantification of blood (A & B) and kidney (C & D) indicate changes in ^{125}I-p5 peptide (arrow; ○) and free ^{125}I (arrowhead; •) over 60 min. (E) SPECT/CT image of WT mouse 30 min post injection of 95 μCi of ^{125}I indicating uptake in the stomach (St) and thyroid (T).

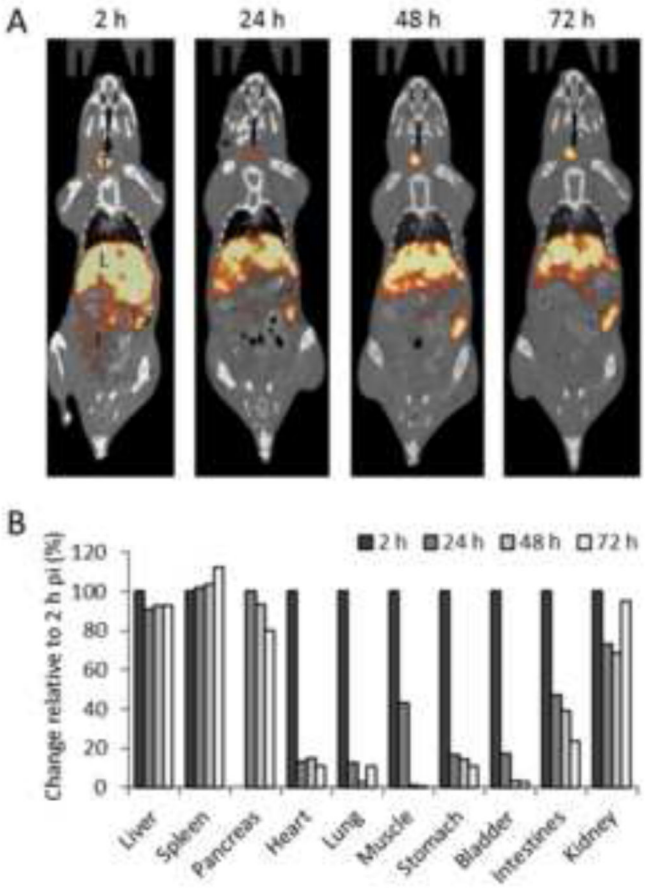

Figure 4.

Longitudinal SPECT/CT imaging of ^{125}I-p5 peptide bound to AA amyloid in mice. A) Representative SPECT/CT images of an individual AA mouse at 2, 24, 48, and 72 h pi of ^{125}I-p5 where L, liver, S, stomach, I, intestines, and T, thyroid. Yellow and red indicate the presence of radioactivity. B) Change in relative radioactivity intensity. The change in SPECT signal intensity was measured by placing ROIs on various tissues and the data expressed as the change relative to the 2 h value, (ratios of means, n = 3). NB: Accurately determining the position of the pancreas in the SPECT images at 2 h pi was not possible. Therefore, changes in this organ were relative to the 24 h time point.

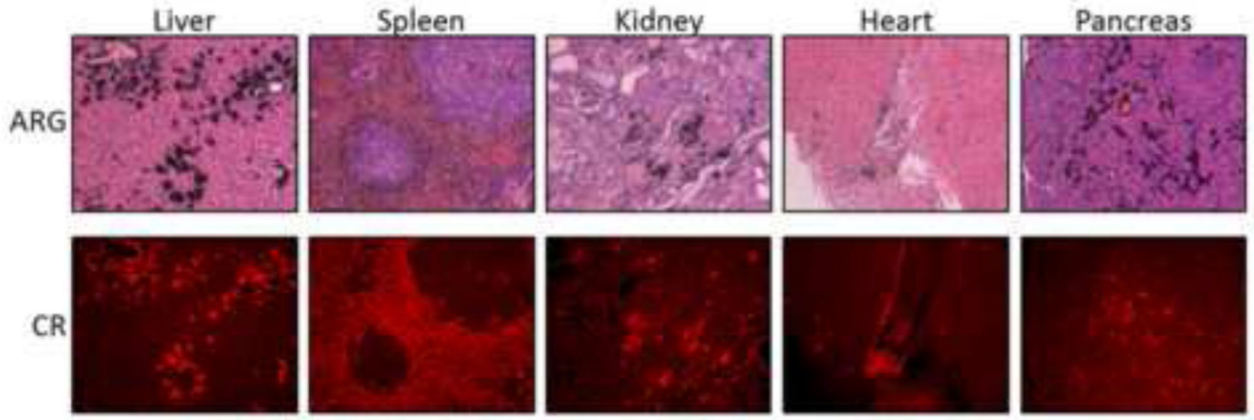

Figure 5.

^{125}I-p5 remains bound to amyloid in vivo at 72 h pi. Microautoradiographs (ARG) show the presence of ^{125}-p5 (black grains) that correlated well with the amyloid distribution as shown by Congo red fluorescence (CR) in a consecutive tissue section.

Table 1

Summary of kinetic parameters.

ROI	WT				AA			
	K_{fast}	K_{slow}	$T1/2_{fast}$	$T1/2_{slow}$	K_{fast}	K_{slow}	$T1/2_{fast}$	$T1/2_{s/c}$
[1]**Blood**	1.88±0.06	0.02±0.01	0.53	37.99	3.9 ±0.12	0.49±0.04	0.49	1.43
[2]**Thyroid**	0.03±0.001	na	20.67	na	nd	na	nd	na
[2]**Kidney**	0.06±0.001	na	10.96	na	0.04±0.003	na	16.62	na
[1]**Liver**	−0.99±0.18	−0.03±0.00	0.70	20.82	2.23±0.12	0.17±0.01	0.31	4.21
[2]**Stomach**	63917±315	na	na	na	8125±173.1	na	na	na
[2]**Spleen**	−0.06±0.01	na	11.19	na	0.04±0.00	na	15.62	na

[1]Double exponential equation fits to the data where, K are the rate constants (min^{-1}: negative indicates exponential decay) and T1/2 (min) the half life of the exponential rate.

[2]single exponential equation fits to the data where, K are the rate constants (min^{-1}: negative indicates exponential decay) and T1/2 (min) the half life of the exponential rate.

[3]Linear equation where Kfast is the slope (Bq/mL/min).